Dependence of microstructure evolution of novel CoreFlow™ aluminium alloy wire on wire diameter

Liang Yuan [a, c], Xun Zeng [b], Xingjian Zhao [b], Yanheng Xie [c], Joao Gandra [d], Dikai Guan [b*]

[a] College of Bioresources Chemical and Materials Engineering, Shaanxi University of Science & Technology, Xi'an, 710021, China

[b] Department of Mechanical Engineering, School of Engineering, University of Southampton, Southampton, SO17 1BJ, UK

[c] Department of Materials Science and Engineering, University of Sheffield, Sheffield, S1 3JD, UK

[d] TWI, Granta Park, Great Abington, Cambridge, CB21 6AL, UK

A B S T R A C T： The wire diameter D_r is one of the key parameters used to tailor the microstructure of alloy wires prepared using a novel room-temperature (RT), one-step CoreFlow™ process. However, the microstructural evolution of CoreFlowed wires at varying D_r remains unclear. The dependence of microstructure characteristics on the D_r should be considered in the future design of CoreFlowed wires. In this study, the microstructure evolution of CoreFlowed 6082 aluminium (Al) wires with four diameters (D_r = 1, 2, 3, and 4 mm) was systematically investigated. After the CoreFlow™, the average grain sizes of all CoreFlowed wires were less than 12 microns compared with the original Al sheet with a coarse grain of 2000 microns. As the D_r increases, the refinement degree of the grain decreases. Particularly, a gradient structure, characterised by grain size increasing from the edge to its centre along the radial diameter, is introduced into CoreFlowed wires. The difference in interaction between strain and heat during CoreFlow™ is responsible for the gradient in grain size. As the D_r increases, the grain size at the edge and its centre increases simultaneously, but the difference in average grain size between them decreases, which is related to the nonlinear change of heat and strain with the D_r. Moreover, the gradient distribution of grain size causes the gradient distribution of specific micro-texture components. The texture components in CoreFlowed wires show a great change with D_r, but their variations show a trend from recrystallization texture to deformation texture with an increase in D_r.

Keywords： CoreFlow™ technology, CoreFlowed Al wire, Wire diameter, Grain refinement, Gradient structure

1. Introduction

The demand for high-performance light alloy wires has shown a surge for various engineering applications, such as load-bearing slings, metallic mesh, welding wire, wire-based additive manufacturing [1-4]. The traditional method of preparing metallic wire consists of a series of complicated steps, including casting [5], extrusion [6], rolling [7], drawing [8], and annealing [9], which require repeated cycles among these steps. Besides, the lengthy traditional processes are almost ineffective in quickly selecting alloy compositions for high performance metallic wires. These drawbacks make traditional wire production methods face a great challenge in terms of energy savings, efficiency improvement, and shortening the research cycle for new alloy wires. Hence, some efforts have been made to optimise the preparation process of the metallic wires, such as the combination processing (extrusion + equal channel angular pressing + hot drawing) [10], the single-step shearing method proposed [11], and the optimized hot- and cold-drawing process [12]. Lately, Chen et al. [13] prepared the high-performance high-entropy alloy (HEA) wires using a well-designed heavy-drawn method, but the elaborately designed process still requires three non-continuous steps, i.e., hot rolling, hot drawing, and cold drawing. Therefore, developing a novel technique that can rapidly fabricate high-performance alloy wire with reduced and continuous steps is urgently required.

Recently, a sub-surface treatment technology developed by the Welding Institute (TWI) with the help of a friction stir processing (FSP) mechanism [14], named CoreFlow^{TM}, is a very promising method for the preparation of alloy wire. Particularly, the CoreFlow^{TM} technique has been proved to produce Mg alloy wires [15], and Al alloy wires [16] from materials with poor extrudability in our previous studies. During the CoreFlow^{TM} process shown in Fig. 1, first, the substrate material undergoes a cutting and extrusion process under the rotation of the thread probe; then, the thermo-mechanically plasticized material is welded together at the end of the thread; and finally, the consolidated material is extruded as it passes through the extrusion hole on the stationary shoulder and is accompanied by air-cooling. The aforementioned entire process can be accomplished in a rapid succession of steps under mild atmospheric conditions, enabling the CoreFlow^{TM} process to be utilized to

fabricate light alloy wire in a RT one-step. A striking feature of the post-CoreFlowed alloy wires is that grain refinement, tailored texture, and redistributed phase particles often decorate their microstructures. These characteristic structures endow the CoreFlowed wire with a variety of unexpected mechanical properties. For instance, Al-Mg-Zr alloy wire prepared using a shear-assisted processing and extrusion technique similar to the CoreFlow^{TM} process exhibits high tensile yield strength (YS) (220 MPa) and high elongation (>20%) [17]. Recently, our work used the novel CoreFlow^{TM} process to prepare CoreFlowed AZ31B wire [15] and CoreFlowed 6082 Al wire [16] from commercial AZ31 plate and 6082-T6 sheet, which all display good RT strength and ductility compared to the original alloy sheet. However, the CoreFlowed AZ31B or 6082 wires with a synergistic combination of YS and ductility have not yet been obtained, which prompts us to further optimize their mechanical properties, since the development of alloy wire with high performance is desired for lightweight design strategies and advanced energy applications.

Our uniaxial tensile results have shown [16] that post-ageing treatment can cause the mechanical properties of CoreFlowed 6082 Al wires to change in a wide range, which provides us with a path to tailor their mechanical properties over a wide range. In addition, EBSD results demonstrated that a gradient structure from the wire edge to its centre was found in the CoreFlowed AZ31B [15]. The typical gradient structure is another possible and promising process for preparing advanced alloy with a synergistic combination of strength and ductility [18, 19], since multiple alloys with gradient structures exhibit excellent strength-ductility synergy [20]. To successfully use the aforementioned two routes to tailor the YS and ductility of CoreFlowed alloy wires, it is key to deeply illustrate the microstructure evolution of the CoreFlowed alloy wires, which was affected by several factors, such as the base materials, rotational speed, the shape of the rotational probe, and the extrusion hole diameter (H_D). In the final extrusion forming stage of CoreFlowed alloy wire, the key parameter H_D dominates the radial dimension (i.e., wire diameter D_r) and strain magnitude of the CoreFlowed alloy wire, which may significantly affect the degree of recrystallization or the distribution width of the gradient structures. At present, however, most studies only focus on the microstructural characterization of the

CoreFlowed alloy wire under a single invariant parameter [21] or at different rotational speeds [22]. The microstructure evolution of the CoreFlowed alloy wires with different D_r values has not yet been systematically investigated, which makes the dependence of microstructure on the D_r values in CoreFlowed wires unclear. On the other hand, the CoreFlow^{TM} technology is still far from being well understood due to its novelty. For a comprehensive understanding of the CoreFlow^{TM} technology, the importance of microstructure evolution in response to the key parameter D_r cannot be ignored.

In this work, the commercial 6082-T6 sheet is selected as the base material due to its maturity and widespread use in engineering applications, and the CoreFlowed 6082 Al wires with four different diameters (D_r=1, 2, 3, and 4 mm) are prepared by controlling the different extrusion hole diameters, as shown in Fig. 2a. Here, we focus on investigating the microstructure evolution of CoreFlowed 6082 Al wires with varying D_r values. Furthermore, the evolution of gradient structures in the CoreFlowed 6082 Al wires with different diameters is also studied in detail.

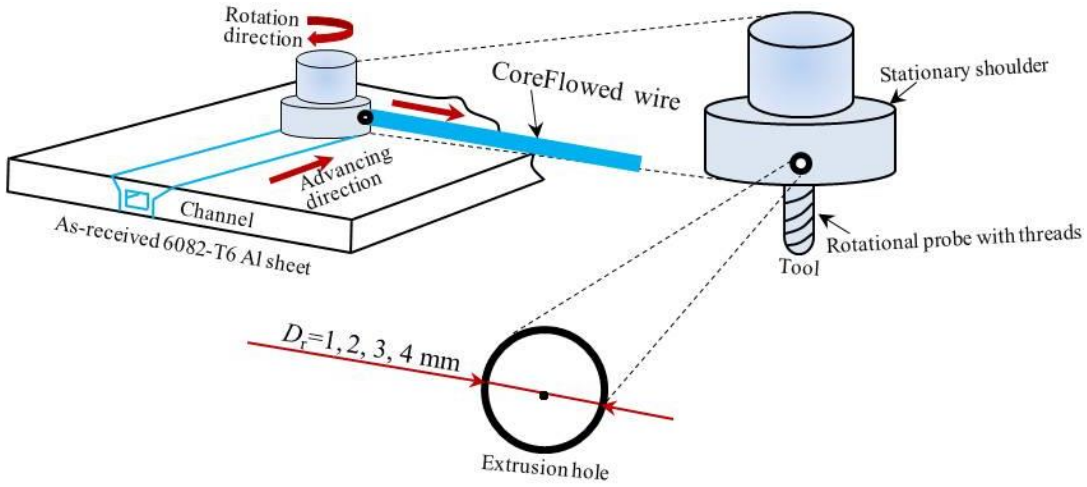

Fig. 1 Schematic diagram of preparing CoreFlowed wires using CoreFlow^{TM}, and the enlarged view of key components.

2. Materials and process

The experimental material used in this study was the commercial AA 6082-T6 Al alloy with the chemical composition of Al-0.88Mg-0.85Si (wt.%) with 0.42Mn, 0.13Fe, 0.03Cu, 0.03Zn, 0.02Cr and 0.02Ti, and their sheets with dimensions of 300 × 300 × 10 mm^3 were used for fabricating the CoreFlowed 6082 Al wires. The 1200 rpm tool

rotational speed was used to produce complete and dense CoreFlowed 6082 Al wire according to our previous experience. Four kinds of CoreFlowed 6082 Al wires with different diameters (D_r=1, 2, 3, and 4 mm) were prepared by replacing the stationary shoulder (Fig. 1) with different H_D values below the tool, i.e., by controlling the corresponding extrusion ratio. Hereinafter, the CoreFlowed 6082 Al wire samples with diameters of 1, 2, 3, and 4 mm are denoted by D_1, D_2, D_3, and D_4, respectively. To explore the effect of the D_r values on the microstructure of CoreFlowed 6082 Al wires, all the other parameters remained the same during the preparation of CoreFlowed 6082 Al wires with different diameters. The macro-views of CoreFlowed 6082 Al wire with different diameters in Fig. 2a show that their entire surface is smooth, and no cold tearing or other defects are found except for a slight twist.

The microstructure of the CoreFlowed Al wires was characterized by scanning electron microscope (SEM, JSM-7900F) equipped with an Oxford Instrument electron back scatter diffraction (EBSD) detector. The step size for EBSD testing is 1 μm. The EBSD samples were obtained from cross sections and longitudinal sections of as-received CoreFlowed Al wires. Considering the experimental period, when the cross section of the different diameters' CoreFlowed Al wires is scanned in EBSD mode, only the test area of the D_1 sample took up a quarter of the cross section, while the test areas of the D_2-D_4 samples extended a small part from the outer contour to the centre of the circle, as shown in Fig. 2b. Although the selected test area marked by light orange is difficult to fully display the microstructure of the entire cross-section, it can still reflect the microstructure changes at the edge and centre of the cross-section. The samples for EBSD analysis were mechanically polished and followed by ion polishing with a Gatan PECS II ion polisher under a condition of 5 kV, 4° for 30 min. The EBSD data was analyzed with the HKL-Channel 5 software (HKL Channel 5.0, Oxford Instrument). To eliminate spurious boundaries caused by orientation noise, the boundary misorientation of less than 2° was cut off. Grain boundaries with misorientation angles θ larger than 15° were defined as high-angle grain boundaries (HAGBs) and those of θ in the range of 2°<θ<15° as low-angle grain boundaries (LAGBs). Meanwhile, the kernel average misorientation (KAM) image was also obtained to a deeper understanding of grain deformation.

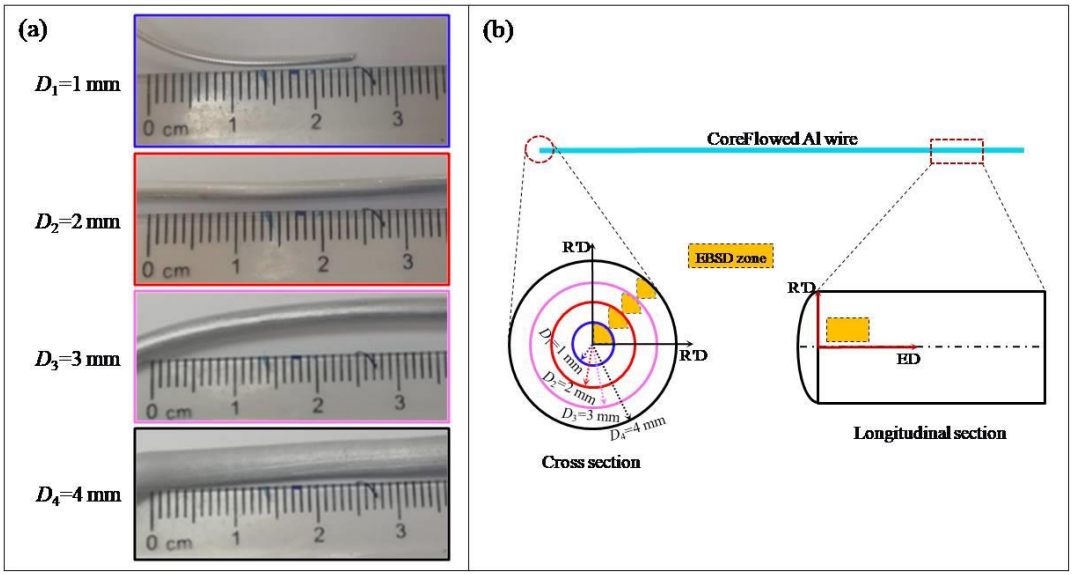

Fig. 2 Macro-views of CoreFlowed 6082 Al wires with different diameters (a), and the corresponding schematic diagram of EBSD testing regions along cross- and longitudinal-sections of CoreFlowed Al wires (b). R'D and ED denote the radial and extrusion direction of CoreFlowed Al wires, respectively.

3. Results

3.1. Grain refinement of CoreFlowed Al wires

To highlight the effect of the CoreFlow™ technology on grain refinement by comparing the grain size between the original 6082-T6 Al alloy sheet and CoreFlowed 6082 Al wires, it is necessary here to give a brief description of the microstructure of the original 6082-T6 Al alloy sheet, although its details have been described in our previous work [16]. The average grain size of the original 6082-T6 Al alloy sheet was measured to be about 100 μm, 2000 μm, and 2000 μm along TD (transverse direction), ND (normal direction), and RD (rolling direction), respectively. Namely, the original 6082-T6 Al alloy sheet consists of coarse and elongated grains.

As a new severe plastic deformation (SPD) technology, the effect of friction stir processing on grain refinement has been reported in previous research, such as in friction extrusion [23], high-speed friction stir [24], and friction-stir extrusion [25]. As shown in Figs. $3a_1$-d_1, there is no abnormal coarse or elongated grain in the CoreFlowed 6082 Al wires with different diameters along the cross section, implying that the dynamic recrystallization was sufficiently activated during the CoreFlow™

process. In other words, the grains of the CoreFlowed 6082 Al wires are completely refined after the CoreFlow™ process compared with the coarse grains of the original 6082-T6 Al alloy sheet. It can be seen from Figs. 3a_3-d_3 that the mean grain sizes of the different CoreFlowed 6082 Al wires along the cross section are reduced to less than 12 μm. With the increase of the D_r from 1 to 4 mm, the grain sizes of the CoreFlowed wires increase gradually. Namely, the average size of refined grain observed from the cross section (Figs. 3a_2-d_2) gradually increased from 7.63 (D_1) to 11.92 μm (D_4) (Figs. 3a_3-d_3), which is visualized in Fig. 5a. The increasing trend of grain sizes with an increase in D_r may be closely related to the stress variable and the heat dissipation rate experienced during the CoreFlow™ process, which has been implied by the relevant simulation results [26].

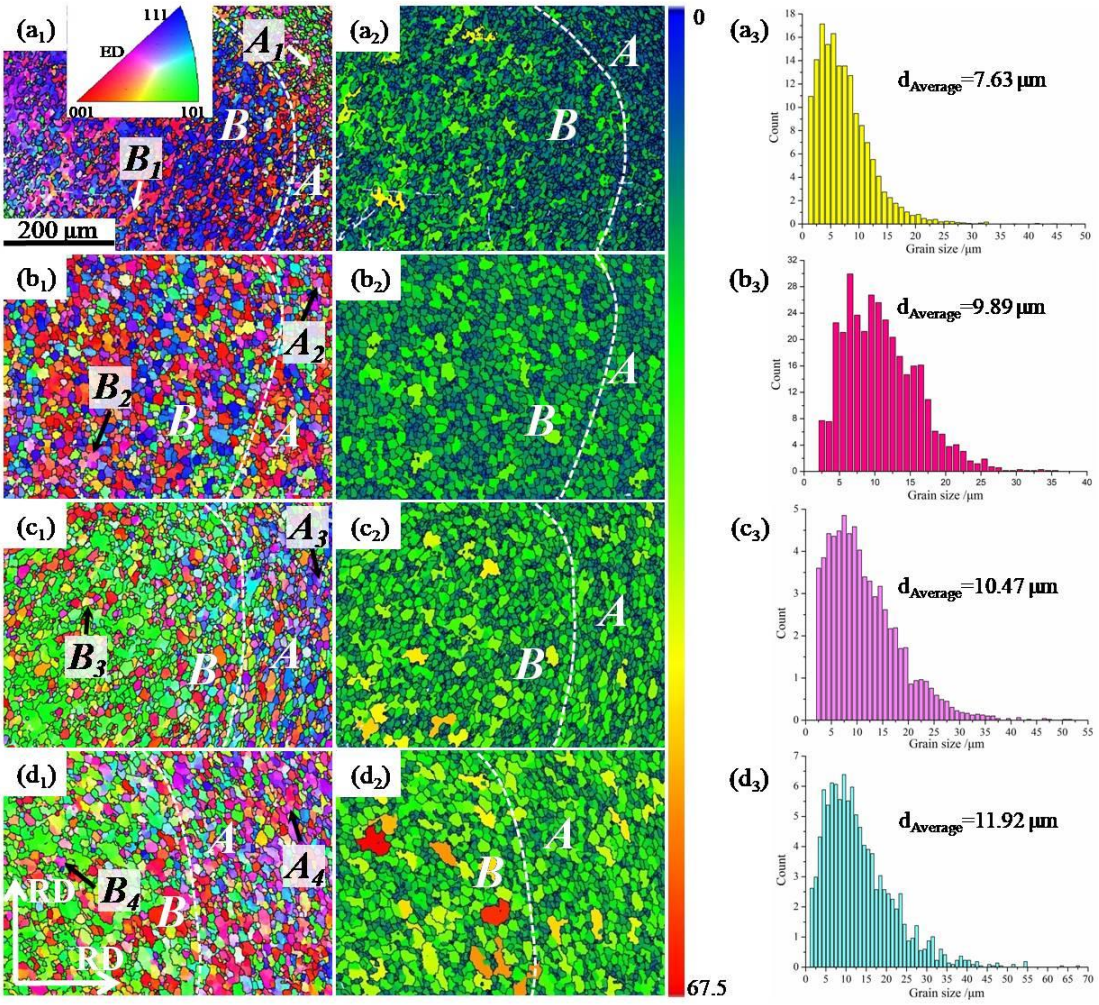

Fig. 3 EBSD Characterization of the different CoreFlowed Al wire samples along the cross section. (a_1-d_1) IPF maps, (a_2-d_2) distribution maps of grain size, (a_3-d_3)

distribution charts of grain size, (a_1-a_3) D_1, (b_1-b_3) D_2, (c_1-c_3) D_3, and (d_1-d_3) D_4.

In addition, it is found in the grain size distribution maps in Figs. $3a_2$-d_2 that a feature characterized by a few large grains embedded in small ones appears in all CoreFlowed 6082 Al wires with different diameters; meanwhile, the number of large grains gradually increases with D_r. The shape of the large grains in the D_1 sample presents an irregular feature that starts to become an equiaxial shape with increasing D_r. Most importantly, both the size and orientation of the grain are significantly inhomogeneous from the edge (marked by *A*) of CoreFlowed 6082 Al wires to their core (marked by *B*). Here, we use a white dotted line to approximate the dividing line between the *A*- and *B*-regions, as shown in Figs. $3a_2$-d_2. In other words, the sizes and orientations of grains are distributed in a gradient from the edge *A* region to the central *B* region. With increasing D_r, it is found that the dividing line between the *A*- and *B*-regions gradually moves towards the core of CoreFlowed 6082 Al wires. Since the gradient distribution of grain size in FSEed AA7277 Al wire after friction-stir extrusion and HEA wires after rolling or drawing processing is attributed to the strain gradient by Behangh et al. [25] and Chen et al. [13], it is reasonable to speculate that this gradient distribution of grain size in the studied CoreFlowed 6082 Al wires is closely related to the complex strain distribution during CoreFlow™ processing. Gradient grains [27], gradient twins [28], gradient stacking faults [29], gradient texture [30], and gradient second phase particles [31] are generally considered for materials design. The gradient grains are the most widely used microstructural regulation method in various metals and alloys for achieving excellent strength-ductility combinations [32]. Since the gradient grain can be obtained flexibly in CoreFlowed 6082 Al wires by tailoring their diameters, more studies should focus on strengthening and deformation mechanisms in CoreFlowed Al wires with a gradient grain in the future.

Figs. $4a_1$-d_1 shows the grain orientation map of CoreFlowed 6082 Al wires along longitudinal section after the CoreFlow™ processing. Remarkably, grains along the longitudinal section of the CoreFlowed 6082 Al wires are also refined compared with those of the original 6082-T6 Al sheet. Figs. $4a_2$-d_2 and $4a_3$-d_3 illustrate the variations of the grain size distribution and its statistical histogram, respectively. When the D_r is

1 mm, the grains in the D_1 sample consist of equiaxed fine grains and elongated irregular grains along the extrusion direction, as shown in Fig. 4a_2. As the D_r value increases to 2 mm, the grains in the CoreFlowed 6082 Al wire are nearly equiaxed (Fig. 4b_2). As the D_r value further goes up to the range of 3-4 mm, the elongated grains begin to appear again around fine equiaxed grains along the extrusion direction (Figs. 4c_2 and d_2). In this stage, the grains are elongated accompanied by the appearance of equiaxed grains. Comparing grain sizes along the cross- and longitudinal-sections, there is an obvious tendency that the grain size of CoreFlowed 6082 Al wires along the cross section is larger than that along the longitudinal section, regardless of the diameter of the CoreFlowed 6082 Al wires (Fig. 5a). Meanwhile, the mean grain size increases more along the cross section than along the longitudinal section with an increase in D_r value.

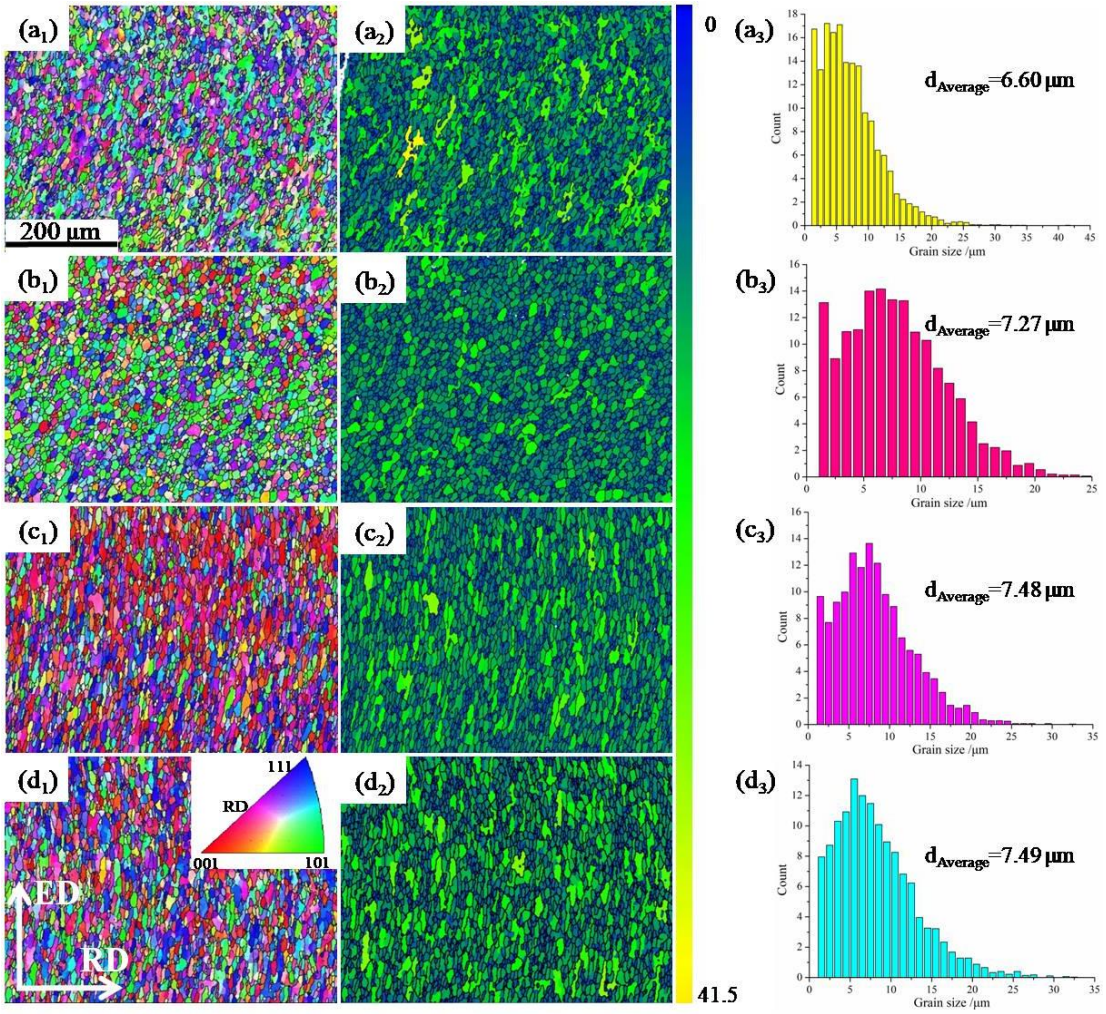

Fig. 4 EBSD Characterization of the different CoreFlowed 6082 Al wire samples

along the longitudinal section. (a_1-d_1) IPF maps, (a_2-d_2) distribution maps of grain size, (a_3-d_3) distribution charts of grain size, (a_1-a_3) D_1, (b_1-b_3) D_2, (c_1-c_3) D_3, and (d_1-d_3) D_4.

Since the grains along the extrusion direction were obviously elongated as the D_r value increased from 2 to 4 mm, we further studied the functional relationship between the thicknesses (t) and lengths (L) of the grains in the CoreFlowed 6082 Al wires and the variation of the D_r value, as shown in Fig. 5b. Clearly, the t value of the grains along the longitudinal section appears to fluctuate slightly as the D_r value increases from 1 to 4 mm. In contrast, the L value of grains decreases first and then dramatically increases with increasing D_r value, which is consistent with the distribution maps of grain size in Figs. 4a_2-d_2. Moreover, it is interesting to note that the color of the individual grains in the CoreFlowed 6082 Al wires shows a gradient change regardless of cross section (Figs. 3a_1-d_1) or longitudinal section (Figs. 4a_1-d_1), indicating the inhomogeneity of the strain during the CoreFlow™ process.

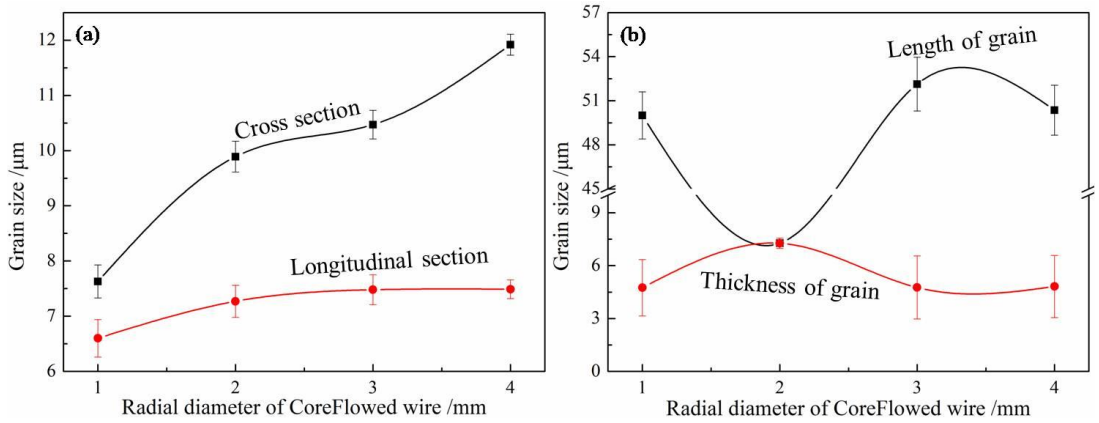

Fig. 5 The evolution of the diameter of the equiaxed grains (a) and the thicknesses and lengths of the elongated grains (b) with the D_r value.

3.2. Gradient distribution of grain sizes along cross section

To our knowledge, the typical gradient distribution of grain size in CoreFlowed 6082 Al alloy wires has not been investigated. To clearly show the gradient evolution characteristics of the grain size in Figs. 3a_2-d_2, the grain size obtained from both edge A and central B regions as a function of the D_r is illustrated in Fig. 6. Obviously, the mean grain sizes of the A region along the cross section are lower than those of the corresponding B region in four kinds of CoreFlowed 6082 Al wires. Namely, a gradient

distribution of the grain sizes of different CoreFlowed 6082 Al wires occurs from the edge to their centre.

As the D_r value increases, the grain size at edge *A* and centre *B* increases gradually, but the difference (Δ) in average grain size between edge *A* and centre *B* decreases, i.e., Δ_1=1.247 μm (D_1=1 mm) > Δ_2=0.4319 μm (D_2=2 mm) > Δ_3=0.1445 μm (D_3=3 mm) > Δ_4=0.0394 μm (D_4=4 mm), indicating that the growth rate of grain in edge *A* was higher than that in centre *B* with the increase in D_r value, which is related to the nonlinear change of heat and strain with the D_r value along the cross section.

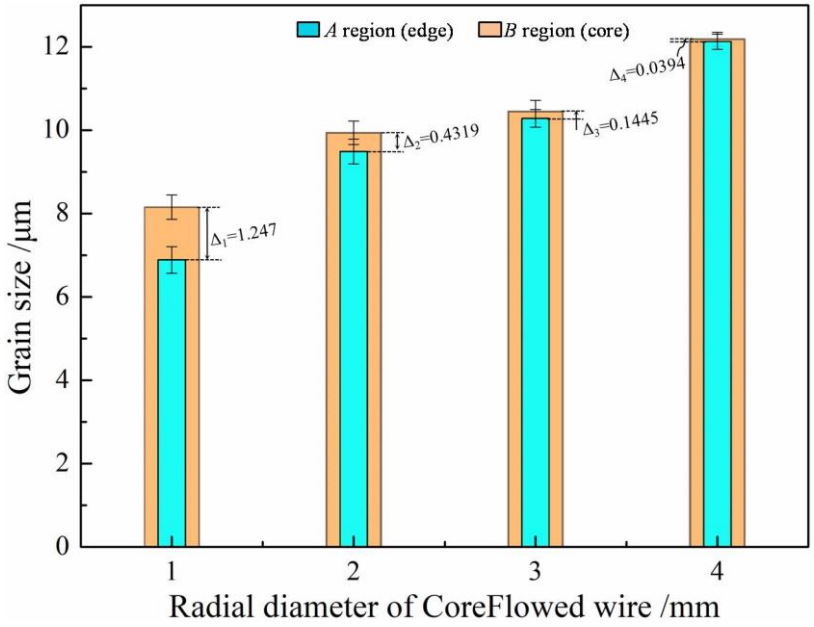

Fig. 6 Histogram of grain size variation with the D_r value in different regions along the cross section.

3.3. Grain boundary characteristics at different wire diameters

The distributions of grain boundary misorientation of CoreFlowed 6082 Al wires along the cross section and longitudinal section are shown in Figs. 7a_1-a_4 and b_1-b_4, respectively, and the corresponding grain boundary maps are shown in Figs. 7c_1-c_4 and d_1-d_4, respectively. The HAGBs' percentage was calculated based on the following equation (1):

$$V_{HAGB} = \frac{N_{HAGB}}{N_{HAGB} + N_{LAGB}} \quad (1)$$

where V_{HAGB} stands for the HAGBs' percentage, N_{HAGB} and N_{LAGB} are the sum of the HAGBs and the LAGBs, respectively. The relationship curve between the HAGBs'

percentage and the D_r value is shown in Fig. 7e after statistics. Clearly, the V_{HAGB} along the cross section increases from 47.70% to 75.14% as the D_r value increases from 1 to 2 mm. When the D_r value increases to 3 mm, however, the V_{HAGB} of CoreFlowed 6082 Al wires decreases from 75.14% to 65.13%. When the D_r value increases again to 4 mm, the V_{HAGB} continues to decrease slowly to 57.53%. From a longitudinal section view, the V_{HAGB} varies consistently along the longitudinal and cross sections when the D_r value varies in the range of 1-2 mm. Nevertheless, when the D_r value increases from 2 to 3 mm, the V_{HAGB} significantly increases to 74.83%, and when the D_r value increases to 4 mm, the V_{HAGB} remains at a high level of 71.35%. These results indicated that the evolution of the misorientation angle is closely related to the recrystallization and formation of sub-grains during the CoreFlow™ process.

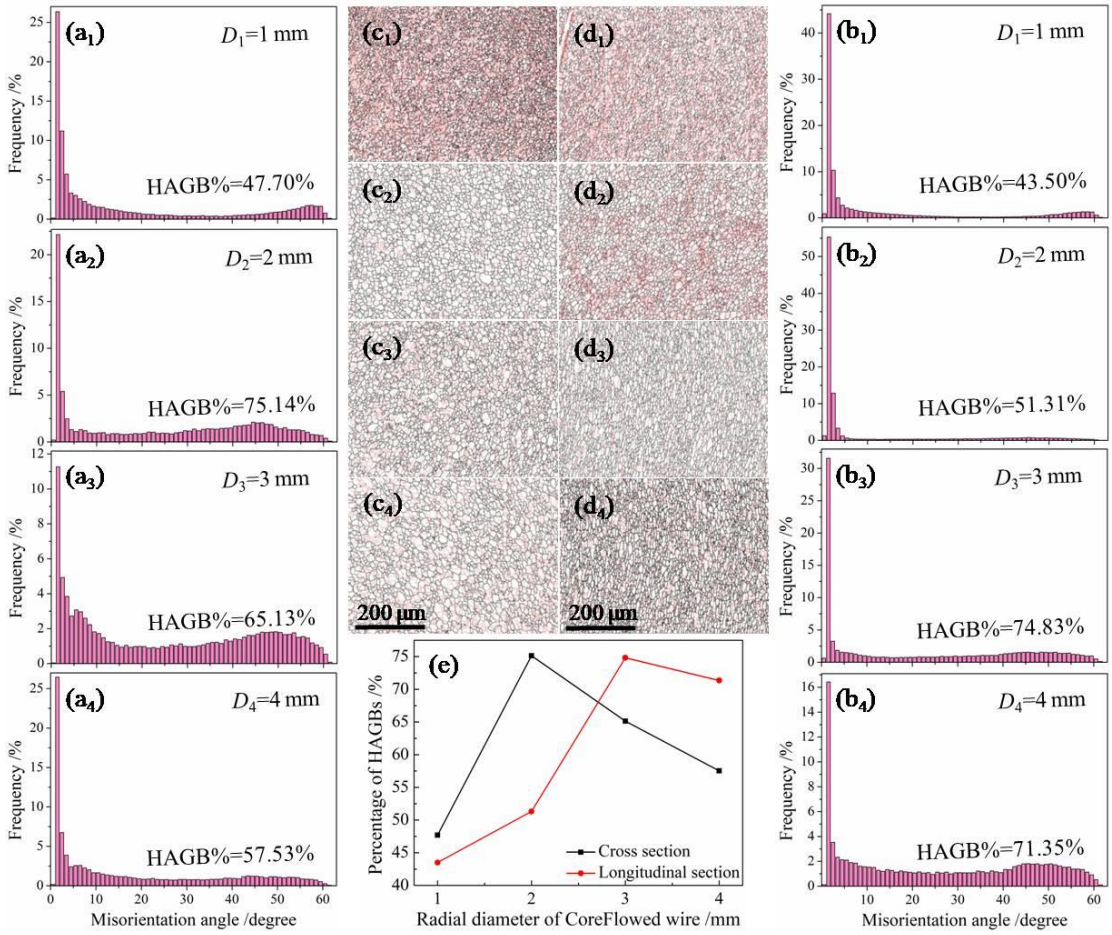

Fig. 7 Misorientation distribution along the cross section (a_1-a_4) and longitudinal section (b_1-b_4), and the corresponding grain boundary maps (c_1-c_4, and d_1-d_4), and the percentage of HAGBs in the CoreFlowed 6082 Al wires with the change in D_r (e).

3.4. Dependence of microtexture evolution on extrusion ratios

To further understand the evolution of grain structure during CoreFlow™, the microtexture evolution of the CoreFlowed Al wires was also analyzed. Here, orientation data were derived from appropriate EBSD maps, arranged as 001 and 111 PFs and summarized in Figs. 8a_1-d_1 and 9a_1-d_1, respectively. For comparison, ideal texture components in face-centred cubic (FCC) metals were also placed in corresponding Figs. 8a_2-d_2 and 9a_2-d_2, respectively. The textures were determined to be (111)[011] and (100)[012] (Fig. 8a_1) in the D_1 sample. Compared with the standard PF of different texture components, the actual texture produced in the process of CoreFlow™ is deflected by about 60° anticlockwise. With the increase in D_r, the dominant texture component in the D_2 sample becomes a single shear {100}<011> texture (Fig. 8b_1). As the D_r value increases further, the texture components mainly include Brass {110}<112> and Copper {211}<111> texture in the D_3 sample (Fig. 8c_1) and D_4 sample (Fig. 8d_1), respectively.

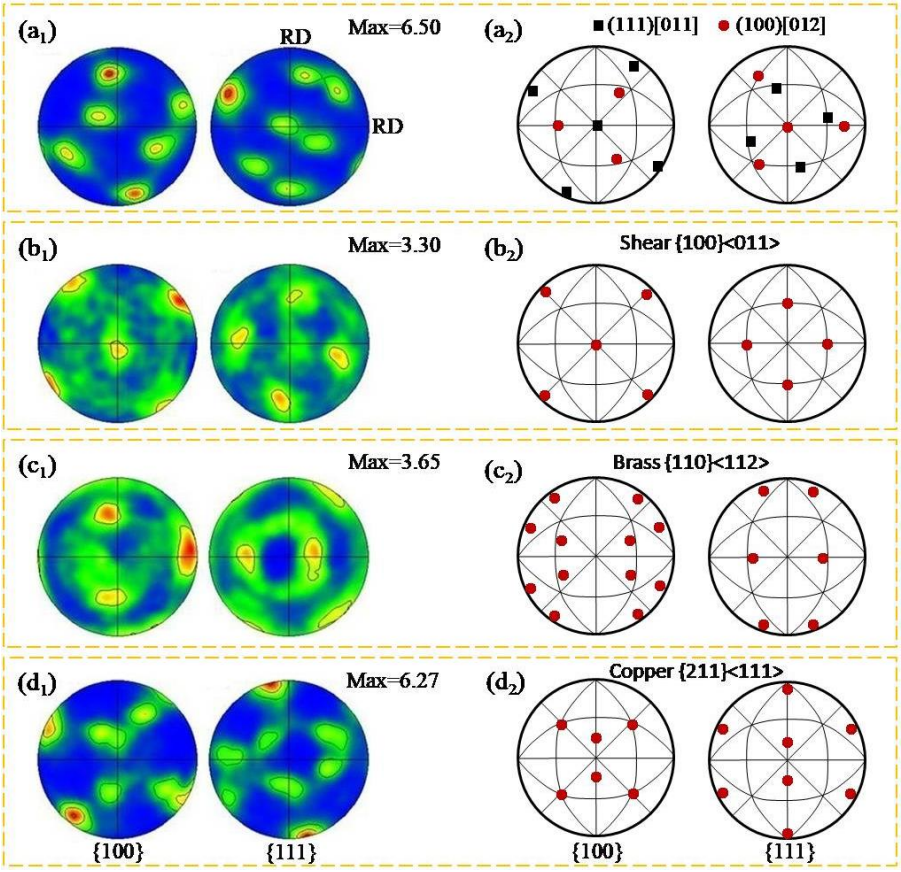

Fig. 8 Pole figures (PFs) of different CoreFlowed 6082 Al wires along cross section. (a_1) D_1, (a_2) D_2, (a_3) D_3, and (a_4) D_4, and the corresponding standard {100}, {111} PF

of texture components in FCC structure (a_2-d_2).

Similarly, the texture components along the longitudinal section also change continuously with the D_r value. The details are that the texture components are (110)[001] and (112)[111] in the D_1 sample (Fig. 9a_1), Goss {110}<001> texture in the D_2 sample (Fig. 9b_1), and Annealing {111}<211> texture in the D_3 (Fig. 9c_1) and D_4 (Fig. 9d_1) samples, respectively. It is worth noting that the double textures in the D_1 sample are deflected anticlockwise by about 30^o against the standard PF of the texture. Although the texture components show diversity in number and type with the change in D_r value after the CoreFlow^{TM} process, the intensity of these texture components is relatively weak on the whole. CoreFlowed 6082 Al wire along the cross and longitudinal sections shows only weak textures with a maximum intensity of less than about 6.50 times and 8.55 times above the random background, respectively. In fact, the texture component properties inherit the characteristics of recrystallization and plastic deformation behavior that depend on heat transfer and stress distribution during the CoreFlow^{TM} process. In fact, the evolution of the texture components aforementioned is consistent with the evolution of grain morphology (Figs. 3 and 5) and grain size (Fig. 4). Namely, the {100}<011> and Goss texture observed in the D_2 sample, is a typical recrystallization texture, leading to the presence of equiaxed grains, while the deformation texture components dominate in the D_1, D_3, and D_4 samples, resulting in the appearance of elongated grains.

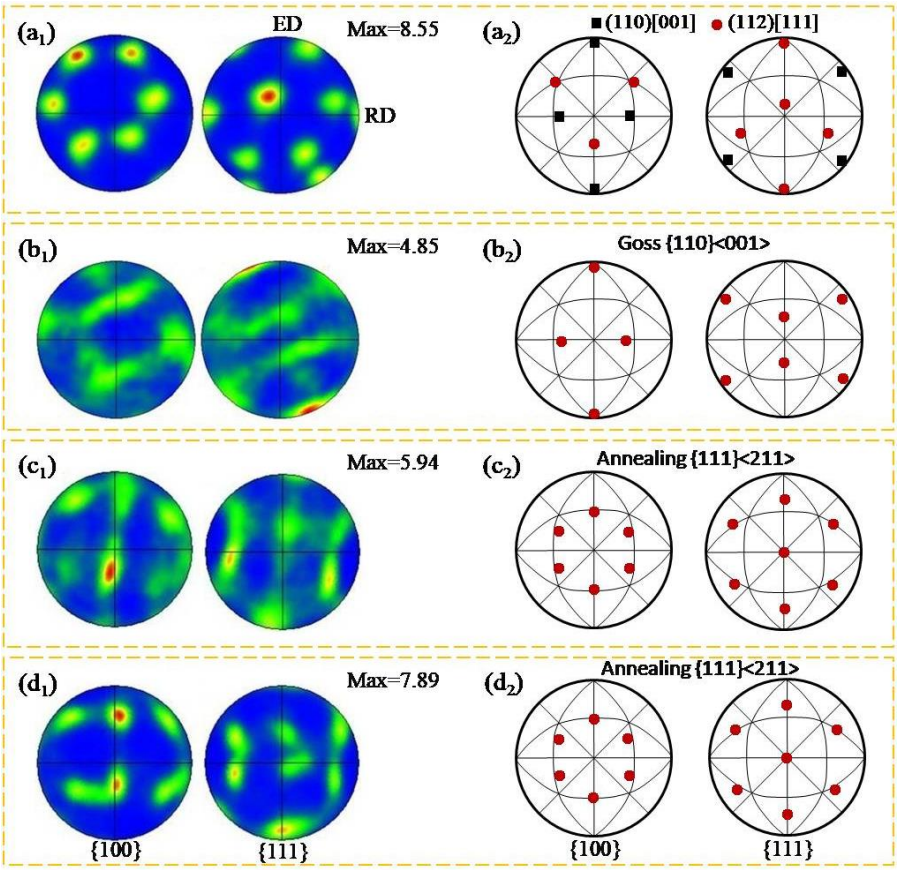

Fig. 9 EBSD-PFs of different CoreFlowed 6082 Al wires along longitudinal section. (a_1) D_1, (a_2) D_2, (a_3) D_3, and (a_4) D_4, and the corresponding standard {100}, {111} PF of texture components in FCC structure (a_2-d_2).

3.5. Gradient distribution of texture components along the radial diameter

Figs. 3a_2-d_2 and Fig. 6 demonstrate that the grain size of the CoreFlowed 6082 Al wires along the cross section exhibits a gradient distribution from the edge to the central regions. The gradient distribution of grain size is closely related to the non-uniform strain during the CoreFlow™ process, which may induce a gradient distribution of the microtexture components. Fig. 10 shows the common texture components in different CoreFlowed wires to verify whether the common texture components along the cross section also present a gradient distribution from the central to edge regions. As shown in Fig. 10a, the shear texture component among the various texture components exhibits a significant gradient distribution in the D_1 sample. With the increase in D_r value, the texture components of Cube, Copper, and Shear show a gradient distribution in the D_2 sample (Fig. 10b). When the D_r value further increases to 3 and 4 mm, the gradient distribution characteristics of texture

components are dominated by Goss, Brass, and Shear in the D_3 (Fig. 10c) and D_4 samples (Fig. 10d).

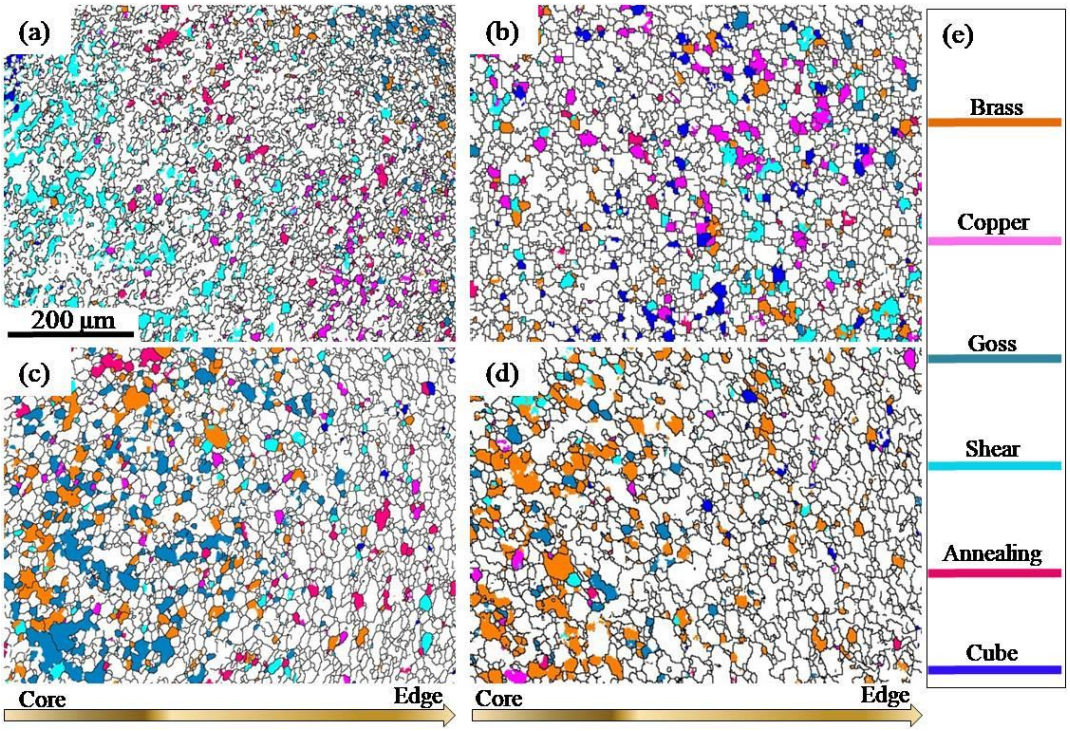

Fig. 10 Texture components maps of different CoreFlowed wires along the cross section. (a) D_1, (b) D_2, (c) D_3, and (d) D_4, and corresponding legend of texture components (e).

3.6. Dislocation density evolution under different wire diameters

Accompanied by severe plastic deformation, dislocation density evolution, which can reflect the strain distribution of the CoreFlowed 6082 Al wires during the CoreFlow™ process, is an important microstructure feature. To study the dislocation density evolution in the CoreFlowed 6082 Al wires with the change in D_r value, the kernel average misorientation (KAM) method is used to determine the local misorientation, which can be further used to calculate the geometrically necessary dislocation (GND) density. Here, we use a simple strain gradient theory method to extrapolate the GND density, as shown in (2):

$$\rho^{GND} = \frac{2\Delta\theta_i}{ub} \tag{2}$$

where ρ^{GND} and $\Delta\theta_i$ represent the GND density at the point of interest and the local misorientation, respectively, u and b are the unit length of the point (u≈100 nm)

and the Burgers vector (b≈2.54 in FCC structure) [33], respectively. According to the principles above, the ATEX software was used to calculate the GND density [34]. Here, take the D_2 sample as an example. Its typical GND density images along the cross and longitudinal sections are shown in Figs. 11a and 11b, respectively. The variation curve of the calculated mean GND density with the D_r value is shown in Fig. 11c. Obviously, the GND density along the cross section decreased rapidly with the increase of the D_r from 1 to 2 mm, and then slightly increased with a further increase of the D_r value. For the longitudinal section, the GND density slightly fluctuated as the D_r value increased from 1 to 2 mm, and then continued to decrease as the D_r value increased from 2 to 4 mm.

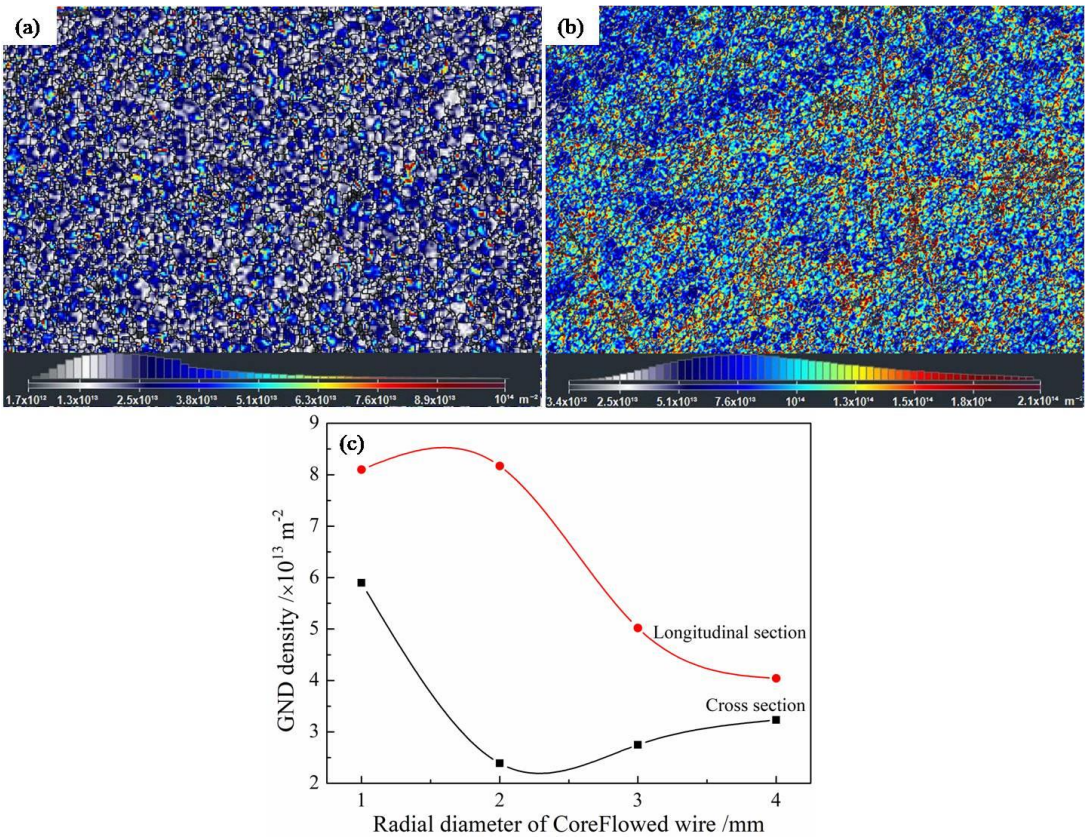

Fig. 11 Typical GND density images of the D_2 sample along cross (a) and longitudinal sections (b), the relationship curve between the mean GND density and the D_r value (c).

4. Discussion

CoreFlow™ processing provides a novel and simple route (i.e., RT one-step) for producing Al alloy wires with refined grains, which is challenging to manufacture

using conventional methods. In addition, the microstructure characteristics of the CoreFlowed alloy wires can be continuously tailored by controlling their D_r values. After large deformation during the CoreFlow^{TM} process, the GND density in the four types of CoreFlowed 6082 Al wires still maintains a relatively low value (the order of 10^{13} in Fig. 8c), which is attributed to the recovery of the dislocations during the thermoplastic deformation due to a relatively high SFE of the Al alloy. The grain structures change obviously with the increasing D_r value. Recent studies have shown that the grain structure plays a key role in influencing the mechanical properties of the CoreFlowed AZ31B alloy wires [15]. Therefore, the microstructure evolution of the different CoreFlowed Al wires will be discussed below.

4.1. Grain refinement

Over the years, the grain refinement behavior in metals and alloys has been well investigated due to its series of beneficial effects on mechanical properties, such as fine-grained strengthening [35], fine-grained superplasticity [36], and fine-grained toughening [37]. As a novel SPD technology, the CoreFlow^{TM} process utilizes friction heat and mechanical forces (shear, tension, and compression) to refine grains directly in a single step by the rotating tool without extra external heat input, showing attractive potential compared with other traditional SPD variants including cold drawing [38], equal-channel angular pressing [39], high pressure torsion [40], and accumulative roll bonding [41], which require multiple repetitive steps as well as extra pre-treatments between steps for the grain refinement. On the other hand, CoreFlowed 6082 Al wires with different diameters (Fig. 2a) can be quickly obtained by adjusting the extrusion hole diameter. Meanwhile, it is theoretically possible to obtain alloy wires of unlimited length as long as the base material is sufficiently large, which breaks the limitation of dimension that the traditional SPD process can only produce small parts of limited dimension [42].

It has been demonstrated by experimental measurements combined with the thermal model predictions that a temperature gradient range of 25-550 ^{o}C occurs in the friction extruded AA-6061 alloy wire during friction extrusion processing (FEP) [2]. Considering the similarity between CoreFlow^{TM} and FEP technology, it is reasonable that the CoreFlowed 6082 Al wires will also experience a high temperature gradient

during the CoreFlow™ process due to the friction stirring heat. The high temperature accompanied by severe plastic deformation under complex material flow is responsible for the grain refinement (Fig. 3 and Fig. 5) through dynamic recovery (DRV) and dynamic recrystallization (DRX) [43] during the CoreFlow™ process. During the high temperature deformation, dislocations inside the grain are rearranged to form LAGBs via glide, climb, and cross-slip [44]. Globular subgrain structures appear with LAGB's separation (Figs. $7c_1$-c_4, and d_1-d_4). As the deformation increases, subgrains become smaller individual grains via continuous dynamic recrystallization (CDRX) and discontinuous dynamic recrystallization (DDRX) [45]. Due to the high stacking fault energy (SFE), the DDRX mechanism is difficult to implement on the currently studied CoreFlowed 6082 Al wires. For the CDRX mechanism, the dislocation near the grain boundary is first rearranged, and then the movable dislocation enters the subgrain boundary, and the trapping of the lattice dislocation on the LAGBs increases its misorientation. Finally, the LAGBs transform into the HAGBs with strain. As shown in Figs. 12a and b, internal grain misorientation and well-defined subgrain boundaries confirmed that the grain refinement of the studied CoreFlowed 6082 Al wires is attributed to the CDRX mechanism.

The continuous increase in misorientation from point to origin, i.e., from M_i/M'_i to N_i/N'_i (i=1-4) (Figs. 12c, d), indicates that the subgrains within the pre-existing grains may progressively increase their misorientation and transform into HAGBs under further plastic deformation. In detail, the point to origin misorientation profile of the D_1-D_3 samples in the *A* region shows multi-peaks with angles (Fig. 12c). The alternating lattice orientation could be described by different subgrains and their rotation with strain [46]. The misorientation profile of the D_4 sample in the *A* region seems to have accumulated across the whole grain, which shows jumps located at about 7, 12, and 20 μm from the original point (Fig. 12c). This type of in-grain misorientation results from the formation of subgrains during dynamic recovery. In the *B* region, according to the characteristics of the point to origin misorientation profile (Fig. 12d), the dynamic recovery seems to be responsible for the in-grain misorientation in the D_1, D_3, and D_4 samples, while both subdivision of the grains and rotation of the subgrains with strain mainly occur in the D_2 sample.

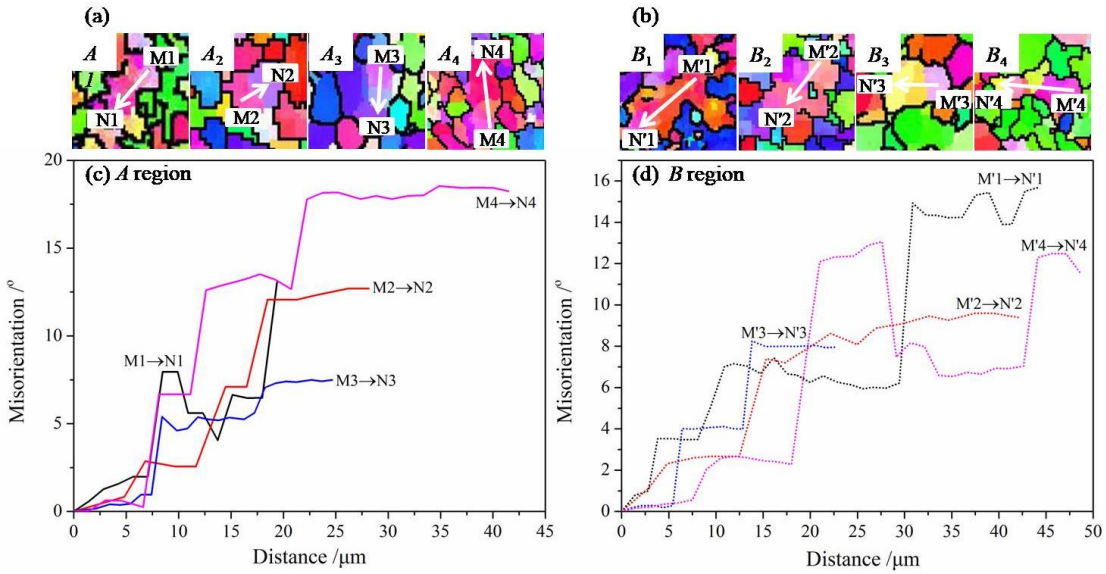

Fig. 12 Enlarged views of the selected grains marked by A_1-A_4 (a) and B_1-B_4 (b) in Figs. 3a_1-d_1, respectively, the corresponding misorientation distribution (c, d) along the arrow in (a) and (b), respectively.

4.2. Gradient characteristics of grain size distribution

The grain size's transition, i.e., the gradient distribution from the edge of CoreFlowed Al wires to their core along the cross section, is attributed to variations in deformation history [13]. As time increases, although the temperature field shows a large gradient, the flow field (velocity, strain rate, and viscosity) still maintains the spatical contour distributions after the extrusion starts [47]. The materials in the central zone experience fewer revolutions and are first pushed out to form the wire, and the central zone is continuously filled by nearby material. The base materials undergo shearing before extruding through the extrusion hole, whose edge zone has suffered higher plastic deformation than its core, which has been confirmed using material tracing technology [48] and the numerical simulation method [47]. In the edge zone of CoreFlowed 6082 Al wires highlighted in label *A* in Figs. 3a_1-d_1, because the frictional heating and shear deformation between the rotating tool and the 6082 Al alloy occur at the edge surface, the input strain was large enough to refine grains in CDRX mode. In contrast, the small shear strain in the core of CoreFlowed Al wires highlighted in label *B* in Figs. 3a_1-d_1 causes some grains to retain their initial size via the DRV process, which has been confirmed by the misorientation distribution in Figs. 9b and d. As a result, the *B* region has a higher mean grain size than the *A* region, as

shown in Fig. 6. Moreover, compared with the grain size at the edge, the core zone may experience grain growth due to a peak temperature, and LAGB by DRV appears due to an insufficient of the input strain in the area. During extrusion, the deformation of the edge material in contact with the mould is greater than that of the inner material. Finally, the alloy wires with a gradient structure characterized by a fine-grain (edge) and a slightly coarser-grain (core) are obtained after friction-stirring extrusion, as shown in Figs. $3a_2$-d_2 and Figs. $5a_2$-d_2.

4.3. Effect of the wire diameter D_r on gradient distribution of grain sizes

After analyzing the dynamic recrystallization behavior of 6082 Al alloy during thermomechanical deformation, Xu et al. [49] proposed a relationship between $-\partial(\ln\theta)/\partial\varepsilon$ and ε with constant strain rate at different temperatures, where θ and ε are work hardening rate and strain, respectively. The diagram of the curve relationship between $-\partial(\ln\theta)/\partial\varepsilon$ and ε is shown in Fig. 13. Clearly, different curves have a minimum point at different temperatures, and the strain at the minimum points can be regarded as the critical strain of dynamic recrystallization. Obviously, the higher the temperature *T*, the smaller the critical strain ε_c of dynamic recrystallization.

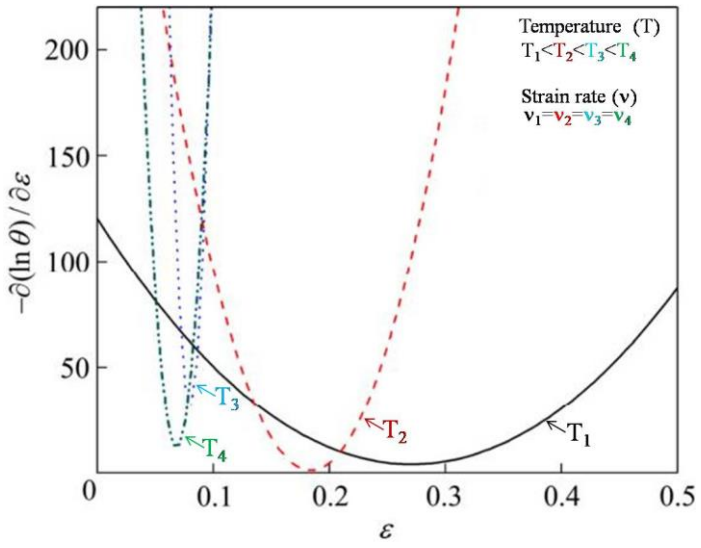

Fig. 13 The relationship curve between $-\partial(\ln\theta)/\partial\varepsilon$ and ε with temperature at constant strain rate.

On the other hand, based on the law of heat transfer, the larger the radial

diameter of the CoreFlowed 6082 Al wires, the higher the heat transfer resistance from inside to outside of the CoreFlowed 6082 Al wires, which leads to a decrease in heat transfer with the increase in CoreFlowed 6082 Al wire diameter after extrusion. Therefore, the temperature sequence of the D_1-D_4 samples is $T_{D4}>T_{D3}>T_{D2}>T_{D1}$ in the stage of CoreFlowed 6082 Al wires from extrusion to air cooling to room temperature, resulting in $\varepsilon_{c\mathrm{E}4} < \varepsilon_{c\mathrm{E}3} < \varepsilon_{c\mathrm{E}2} < \varepsilon_{c\mathrm{E}1}$. However, owing to the decreasing of the recrystallization driving force from the D_1 to D_4 samples during the extrusion with the increase in D_r, the order of the critical strain $\varepsilon_c^{'}$ of recrystallization caused by different strains is $\varepsilon_{c\mathrm{D}_1}^{'} < \varepsilon_{cD_2}^{'} < \varepsilon_{cD_3}^{'} < \varepsilon_{cD_4}^{'}$. Although the ε_c relationship induced by the above two factors of heat transfer and deformation is competitive, the influence of deformation on recrystallization nucleation rate is stronger than that on grain growth based on the relation of recrystallization grain size [49], $d = c\left(G/N\right)^{\frac{1}{4}}$, where d, N and G are grain size, nucleation rate, and growth rate, respectively, and c is a material constant. As a result, the minimum average grain size appears in the D_1 sample, and the maximum average grain size appears in the D_4 sample, which is in agreement with the results in Fig. 4a and Fig. 6. As we know, the degree of dynamic recrystallization depends on both the temperature distribution and the strain magnitude [50]. Although the D_1 sample is subjected to the maximum strain among the four types of CoreFlowed Al wires, it would experience the fastest heat losses during extrusion due to its smallest diameter. The D_3 and D_4 samples with the larger diameter can delay heat loss from centre to edge during extrusion, but their strains during extrusion are relatively small. In contrast, the condition of the D_2 sample falls between D_1 and D_3 or D_4, regarding strain and heat loss. According to the changes in both strain and heat loss in the CoreFlowed wires with four different diameters, the change in grain sizes along the longitudinal section with the D_r will exhibit the characteristics shown in Fig. 4b.

4.4. Evolution of micro-texture components under different wire diameters

4.4.1. Texture components along cross section

When the D_r value is 1 mm, the texture of the D_1 sample consists of a {111}<110> shear texture and a {100}<012> orientation (Figs. 8a_1, a_2). The appearance of the

shear texture indicated that the shear stress along the pin surface causes the plastic flow. As a result, the shear plane and shear direction were roughly parallel to the pin surface and the rotating direction of the tool. In other words, the strain was quite large during the preparation of the D_1 sample. The transformation of 40 degrees <111> grains into the 20 degrees-ED-rotated-cube orientation is responsible for the appearance of the (100)[012] orientation. Moreover, the frequent slip on {100} planes induced by the high values of SFE at higher temperatures is also responsible for the activation of the (100)[012] orientation. In the D_2 sample, the {100}<011> (Figs. 8b_1, b_2) derived from a 40^o <111> orientation is related to the main rolling texture orientations. As the D_r increases further, the plastic deformation of the CoreFlowed 6082 Al wires decreases during extrusion, which reduces the driving force of recrystallization. As a result, more oriented grains caused by deformation are retained. The rolling and extrusion textures of single crystals with FCC structure indicate that the orientations {110}<112> and {112}<111> are rather stable in FCC metals with high SFE [51]. In addition, FCC metals and alloys with high SFE often favor the appearance of the copper-type texture, while the copper (C) {112}<111> component and the brass (B) {110}<112> component are present in nearly equal proportions [52]. Therefore, it is not surprising that the brass {110}<112> and copper {211}<111> texture components appear in the D_3 (Figs. 8c_1, c_2,) and D_4 (Figs. 8d_1, and d_2) samples.

4.4.2. Texture components along longitudinal section

The grains in the D_1 and D_2 samples mainly experienced dynamic recovery and recrystallization due to large plastic deformation under large D_r value. The dislocation energy is a major driving force for recrystallization, which is different from the driving force of grain boundary energy required for grain growth. Here, we discuss the formation of recrystallization texture in the D_1 and D_2 samples based on the strain-energy-release maximization model [53]. Once recrystallization occurs, new grain growth will be controlled by boundary energy. Thus, the recrystallization texture differs from the texture contributed by grain growth. In fact, the recrystallization texture is determined by the absolute maximum internal stress direction that takes all active slip directions into account, which is parallel to the

<100> directions with the minimum Young's modulus for recrystallized grain in FCC metals. As a result, the recrystallized grains generally show a (hk0)[001] orientation. Considering that the (110) plane is shared by the deformed and recrystallized grains, the minimum atomic shuffle condition results in the (110)[001] orientation. Hence, the texture developed in the D_1 and D_2 samples will be dominated by {110}<001> Goss texture (Figs. 9a_1, a_2, b_1, and b_2). A small amount of (112)[111] texture in the E_1 sample is attributed to the residual of the {112}<111> orientation (Figs. 9a_1, a_2) caused by β fiber under higher deformation degrees due to rapid heat dissipation. Heat stays in the D_3 and D_4 samples longer during the process from extrusion to air cooling due to the increasing diameter of the CoreFlowed wire, which corresponds to static recrystallization of deformed grains, inducing an annealing texture {111}<211> (Figs. 9a_3, a_4, b_3, and b_4).

5. Conclusions

In the work, to clarify the dependence of the microstructures of the CoreFlowed wires on the wire diameter D_r during the CoreFlow™ process, CoreFlowed 6082 Al wires with different D_r values (D_r=1, 2, 3, and 4 mm) are prepared by controlling the extrusion hole dimension. The results show that the microstructure of CoreFlowed Al wires, especially the grain size and its distribution, is significantly dependent on the parameter D_r. The strong correlation between the grain structure's evolution and D_r value indicates that the microstructure of CoreFlowed Al wires can be well tailored by controlling D_r value. The gradient structures, including grain size and grain orientation, occur in the CoreFlowed 6082 Al wires along the cross section. The evolution of the structural features in different CoreFlowed Al wires is investigated in detail. The key findings are summarized as follows:

(1) Compared with the coarse-grained 6082-T6 Al sheet, the refinement effect of the CoreFlow™ process on the grain of CoreFlowed Al wires is significant, regardless of wire diameters. After continuous dynamic recrystallization, the grain sizes obtained under four D_r values are all less than 12 microns, but the refined grains gradually become larger with the increase in D_r value.

(2) A gradient grain structure, characterised by its size increasing from the edge to its centre along the radial diameter, is introduced into CoreFlowed Al wires.

With increasing D_r value, the dividing line between the edge region and the centre region gradually moves towards the core of CoreFlowed Al wires. The gradient in grain size is attributed to the coupling of strain and heat during CoreFlow™ processing.

(3) As the diameter D_r value increases, the grain size in both the edge and centre regions increases gradually, but the former increases faster than the latter, which is related to the nonlinear change of heat and strain with the increase in D_r value along the cross section.

(4) The gradient distribution of some specific texture components also appears from the edge of CoreFlowed 6082 Al wires to their centre. With the increase in D_r value, the evolution sequence of dominant texture components with gradient distribution is: Shear (D_r=1 mm) → Cube+Copper+Shear (D_r=2 mm) → Goss+Brass+Shear (D_r=3, 4 mm). Although the micro-texture components in CoreFlowed 6082 Al wires show a great change with the change in D_r value, their variations show a general trend from recrystallization texture to deformation texture with the increase in D_r value.

Credit authorship contribution statement

Liang Yuan: Methodology, Investigation, Formal analysis, Writing-original draft, Funding acquisition, Xun Zeng: Investigation, Formal analysis, Data curation, Xingjian Zhao: Methodology, Investigation, Formal analysis, Data curation, Yanheng Xie: Investigation, Formal analysis, Joao Gandra: Formal analysis, Data curation, Dikai Guan: Conceptualization, Funding acquisition, Supervision, Project administration, Writing-Review & Editing.

Data availability

The data supporting the findings of this study are available from the corresponding author on request.

Declaration of Competing Interest

The authors declare the following financial interests/personal relationships which may be considered as potential competing interests: Dikai Guan reports financial

support was provided by the UKRI MRC Future Leaders Fellowship. Liang Yuan reports financial support was provided by the China Scholarship Council (CSC) Fellowship.

Acknowledgements

The authors appreciate the support from the UKRI MRC Future Leaders Fellowship (Grant No. MR/T019123/2) and the China Scholarship Council Fellowship (Grant No. 201908610075).

R E F E R E N C E S

[1] Zhang X, Hansen N, Godfrey A, Huang X. Dislocation-based plasticity and strengthening mechanisms in sub-20 nm lamellar structures in pearlitic steel wire. Acta Mater 2016; 114: 176-183.

[2] Zhang XY, Yang WX, Xiao RS. Microstructure and mechanical properties of laser beam welded Al-Li alloy 2060 with Al-Mg filler wire. Mater Des 2015; 88: 446-450.

[3] Zhang X, Godfrey A, Huang X, Hansen N, Liu Q. Microstructure and strengthening mechanisms in cold-drawn pearlitic steel wire. Acta Mater 2011; 59: 3422-3430.

[4] Hou JP, Li R, Wang Q, Yu HY, Zhang ZJ, Chen QY, et al. Breaking the trade-off relation of strength and electrical conductivity in pure Al wire by controlling texture and grain boundary. J Alloys Compd 2018; 769: 96-109.

[5] Belov NA, Akopyan TK, Korotova NO, Shurkin PK, Timofeev VN, Raznitsyn OA, et al. Structure and heat resistance of high strength Al-3.3%Cu-2.5%Mn-0.5%Zr (wt%) conductive wire alloy manufactured by electromagnetic casting. J Alloys Compd 2021; 891: 161948.

[6] Gao M, Etim IP, Yang K, Tan LL, Ma Z. Enhancing mechanical property and corrosion resistance of Mg-Zn-Nd alloy wire by a combination of SPD techniques, extrusion and hot drawing. Mater Sci Eng A 2022; 829: 142058.

[7] Hou JP, Wang Q, Yang HJ, Wu XM, Li CH, Li XW, et al. Microstructure evolution and strengthening mechanisms of cold-drawn commercially pure aluminum wire. Mater Sci Eng A 2015; 639: 103-106.

[8] Cheng C, Song KX, Mi XJ, Wu BA, Xiao Z, Xie HF, et al. Microstructural evolution

and properties of Cu-20 wt% Ag alloy wire by multi-pass continuous drawing. Nanotechnol Rev 2020; 9: 1359-1367.

[9] Prasad MJNV, Reiterer MW, Kumar KS. Microstructure and mechanical behavior of annealed MP35N alloy wire. Mater Sci Eng A 2015; 636: 340-351.

[10] Yan K, Sun JP, Bai J, Liu H, Huang X, Jin ZY, et al. Preparation of a high strength and high ductility Mg-6Zn alloy wire by combination of ECAP and hot drawing. Mater Sci Eng A 2019; 739: 513-518.

[11] Issahap MN, Chandrasekar S, Trumble KP. Single-step shear-based deformation processing of electrical conductor wires. J Manuf Sci Eng 2021; 143: 051010.

[12] Piotr K, Andrij M, Dorota B, Olexandr G, Mirko S. The process of ultra-fine wire drawing for magnesium alloy with the guaranteed restoration of ductility between passes. J Mater Process Technol 2017; 247: 234-242.

[13] Chen JX, Li T, Chen Y, Cao FH, Wang HY, Dai LH. Ultra-strong heavy-drawn eutectic high entropy alloy wire. Acta Mater 2023; 243: 118515.

[14] Avettand-Fènoël MN, Netto N, Simar A, Marinova M, Taillard R. Design of a metallic glass dispersion in pure copper by friction stir processing. J Alloys Compd 2022; 907: 164522.

[15] Zhao XJ, Zeng X, Yuan L, Gandra J, Hayat Q, Bai MW, et al. A novel approach for producing Mg-3Al-1Zn-0.2Mn alloy wire with a promising combination of strength and ductility using CoreFlow™. Scripta Mater 2023; 227: 115301.

[16] Yuan L, Zeng X, Zhao XJ, Xie YH, Gandra J, Guan DK. Microstructure evolution and tensile behavior of fine-grained 6082 Al wire with high ultimate strength and high work hardening by friction stir extrusion of bulk Al sheet. Mater Sci Eng A 2023; 864: 144589.

[17] Croteau JR, Jung J, Whalen SA, Darsell J, Mello A, Holstine D, et al. Ultrafine-grained Al-Mg-Zr alloy processed by shear-assisted extrusion with high thermal stability. Scripta Mater 2020; 186: 326-330.

[18] Fang TH, Tao NR. Martensitic transformation dominated tensile plastic deformation of nanograins in a gradient nanostructured 316L stainless steel. Acta Mater 2023; 248: 118780.

[19] Liu MW, Gong W, Zheng RX, Li J, Zhang Z, Gao S, et al. Achieving excellent

mechanical properties in type 316 stainless steel by tailoring grain size in homogeneously recovered or recrystallized nanostructures. Acta Mater 2022; 226: 117629.

[20] Fan JT, Ji XB, Fu LM, Wang J, Ma S, Sun YL, et al. Achieving exceptional strength-ductility synergy in a complex-concentrated alloy via architected heterogeneous grains and nano-sized precipitates. Int J Plast 2022; 157: 103398.

[21] Li JC, Meng XC, Li YL, Wan L, Huang YX. Friction stir extrusion for fabricating Mg-RE alloys with high strength and ductility. Mater Lett 2021; 289: 129414.

[22] Jamali G, Nourouzi S, Jamaati R. FSBE process: a technique for fabrication of aluminum wire with randomly oriented fine grains. Mater Lett 2019; 241: 68-71.

[23] Li X, Tang W, Reynolds AP, Tayon WA, Brice CA. Strain and texture in friction extrusion of aluminum wire. J Mater Process Technol 2016; 229: 191-198.

[24] Naumov A, Morozova I, Rylkov E, Obrosov A, Isupov F, Michailov V, et al. Metallurgical and mechanical characterization of high-speed friction stir welded AA 6082-T6 aluminum alloy. Mater 2019; 4211: 1-16.

[25] Behangh RA, Mahdavinejad R, Yavari A, Abdollahi M, Narvan M. Production of wire from AA7277 aluminum chips via friction-stir extrusion (FSE). Metall Mater Trans B 2014; 45: 1484-1489.

[26] Zhang H, Li X, Tang W, Deng X, Reynolds AP, Sutton MA. Heat transfer modeling of the friction extrusion process. J Mater Process Technol 2015; 221: 21-30.

[27] Fang TH, Li WL, Tao NR, Lu K. Revealing extraordinary intrinsic tensile plasticity in gradient nano-grained copper. Science 2011; 331: 1587-1590.

[28] Wei YJ, Li YQ, Zhu LC, Liu Y, Lei XQ, Wang G, et al. Evading the strength-ductility trade-off dilemma in steel through gradient hierarchical nanotwins. Nat. Commun 2014; 5: 3580.

[29] Pan QS, Yang MX, Feng R, Chuang AC, An K, Liaw PK, et al. Atomic faulting induced exceptional cryogenic strain hardening in gradient cell-structured alloy. Science 2023; 382: 185-190.

[30] Wu D, Hao MY, Zhang TL, Wang Z, Wang J, Rao GH, et al. Heterostructures enhance simultaneously strength and ductility of a commercial titanium alloy. Acta Mater 2023; 257: 119182.

[31] Guo N, Zhang ZM, Dong QS, Yu HB, Song B, Chai LJ, et al. Strengthening and toughening austenitic steel by introducing gradient martensite via cyclic forward/reverse torsion. Mater Des 2018; 143: 150-159.

[32] Wang YF, Wang MS, Fang XT, Guo FJ, Liu HQ, Scattergood RO, et al. Extra strengthening in a coarse/ultrafine grained laminate: role of gradient interfaces. Int J Plast 2019; 123: 196-207.

[33] Xiong T, Zheng S, Pang J, Ma X. High-strength and high-ductility AlCoCrFeNi2.1 eutectic high-entropy alloy achieved via precipitation strengthening in a heterogeneous structure. Scr Mater 2020; 186: 336-340.

[34] Beausir B, Fundenberger JJ. Analysis tools for electron and X-ray diffraction, ATEX - software, www.atex-software.eu, Université de Lorraine - Metz, 2017.

[35] Shi PJ, Zhong YB, Li Y, Ren WL, Zheng TX, Shen Z, et al. Multistage work hardening assisted by multi-type twinning in ultrafine-grained heterostructural eutectic high-entropy alloys. Mater Today 2020; 41: 62-71.

[36] Song ZZ, Niu RM, Cui XY, Bobruk EV, Murashkin MY, Enikeev NA, et al. Mechanism of room-temperature superplasticity in ultrafine-grained Al-Zn alloys. Acta Mater 2023; 246: 118671.

[37] Li R, Li B, Chen X, Wang J, Yan FX, Wang T, et al. Enhanced fracture toughness and toughening mechanisms of fine-grained Mo-12Si-8.5B alloy with a bi-modally structured α-Mo grain. Mater Sci Eng A 2020; 772: 138684.

[38] Huang S, Hu J, Li XY, Liu JM, Liu KK, Qin HY, et al. Influence of deformation degree at cold drawing on structure-properties relationship of a Fe-Ni-Cr superalloy. J Alloys Compd 2023; 930: 167407.

[39] Shahmir H, Mousavi T, He JY, Lu ZP, Kawasaki M, Langdon TG. Microstructure and properties of a CoCrFeNiMn high-entropy alloy processed by equal-channel angular pressing. Mater Sci Eng A 2017; 705: 411-419.

[40] Heidarzadeh A, Neikter M, Enikeev N, Cui LQ, Forouzan F, Mousavian RT. Post-treatment of additively manufactured Fe-Cr-Ni stainless steels by high pressure torsion: TRIP effect. Mater Sci Eng A 2021; 811: 141086.

[41] Verstraete K, Prévond L, Helbert AL, Baudin T. Magnetic shielding at low frequencies: application for an aluminum/steel composite elaborated by

accumulative roll bonding. Adv Eng Mater 2019; 21: 1800967.

[42] Valiev RZ, Murashkin MY, Sabirov I. A nanostructural design to produce high-strength Al alloys with enhanced electrical conductivity. Scripta Mater 2014; 76: 13-16.

[43] Sakai T, Belyakov A, Kaibyshev R, Miura H, Jonas JJ. Dynamic and post-dynamic recrystallization under hot, cold and severe plastic deformation conditions. Prog Mater Sci 2014; 60: 130-207.

[44] Guan RG, Tie D, Li Z, An YN, Wang X, Li Q, et al. Microstructure evolution and mechanical property improvement of aluminum alloys with high magnesium content during continuous rheo-extrusion. Mater Sci Eng A 2018; 738: 31-37.

[45] Jiang MG, Xu C, Yan H, Fan GH, Nakata T, Lao CS, et al. Unveiling the formation of basal texture variations based on twinning and dynamic recrystallization in AZ31 magnesium alloy during extrusion. Acta Mater 2018; 157: 53-71.

[46] Zhao ZB, Wang QJ, Liu JR, Yang R. Characterizations of microstructure and crystallographic orientation in a near-α titanium alloy billet. J Alloys Compd 2017; 712: 179-184.

[47] Zhang H, Li X, Deng X, Reynolds AP, Sutton MA. Numerical simulation of friction extrusion process. J Mater Process Technol 2018; 253: 17-26.

[48] Chen SJ, Han Y, Jiang XQ, Li XX, Yuan T, Jiang W, et al. Study on in-situ material flow behavior during friction stir welding via a novel material tracing technology. J Mater Process Technol 2021; 297: 117205.

[49] Xu ZY, Hu DC. Dynamic recrystallization behavior of 6082 aluminum alloy during hot deformation. Chin J Nonferrous Met 2020; 30: 1231-1237.

[50] Mozumder YH, Babu KA, Saha R, Sarma VS, Mandal S. Dynamic microstructural evolution and recrystallization mechanism during hot deformation of intermetallic-hardened duplex lightweight steel. Mater Sci Eng A 2020; 788: 139613.

[51] Onuki Y, Hongo R, Okayasu K, Fukutomi H. Texture development in Fe-3.0 mass% Si during high-temperature deformation: examination of the preferential dynamic grain growth mechanism. Acta Mater 2013; 61: 1294-1302.

[52] Leffers T, Ray RK. The brass-type texture and its deviation from the copper-type

texture. Prog Mater Sci 2009; 54: 351-396.

[53] Lee DN. Strain energy release maximization model for evolution of recrystallization textures. Int J Mech Sci 2000; 42: 1645-1678.